JOURNAL OF GEOPHYSICAL RESEARCH, VOL. 104, NO. B7, PAGES 15,207–15,226, JULY 10, 1999

The development of slabs in the upper mantle: Insights from numerical and laboratory experiments

Thorsten W. Becker, Caludio Faccenna,[1] and Richard J. O'Connell

Department of Earth and Planetary Sciences, Harvard University, Cambridge, Massachusetts

Domenico Giardini

Institute of Geophysics, Eidgenössische Technische Hochschule, Zurich, Switzerland

Abstract. We have performed numerical and laboratory experiments to model subduction of oceanic lithosphere in the upper mantle from its beginnings as a gravitational instability to the fully developed slab. A two-dimensional finite element code is applied to model Newtonian creep in the numerical experiments. Scaled analog media are used in the laboratory, a sand mixture models the brittle crust, silicone putty simulates creep in the lower crust and mantle lithosphere, and glucose syrup is the asthenosphere analog. Both model approaches show similar results and reproduce first-order observations of the subduction process in nature based on density and viscosity heterogeneities in a Stokes flow model. Subduction nucleates slowly and a pronounced slab forms only when the viscosity contrast between oceanic plate and mantle is below a threshold. We find that the subduction velocity and angle are time-dependent and increase roughly exponentially over tens of millions of years before the slab reaches the 670-km discontinuity. The style of subduction is controlled by the prescribed velocity of convergence, the density contrast between the plates, and the viscosity contrast between the oceanic plate and the mantle. These factors can be combined in the buoyancy number F which expresses the ratio between driving slab pull and resisting viscous dissipation in the oceanic plate. Variations in F control the stress in the plates, the speed and the dip of subduction, and the rate of trench retreat, reproducing the contrasting styles of subduction observed in nature. The subduction rate is strongly influenced by the work of bending the lithosphere as it subducts.

1. Introduction

Wadati-Benioff and high seismic velocity zones indicate that oceanic lithosphere sinks into the mantle, attaining various shapes and suffering contrasting modes of deformation [*Isacks and Molnar*, 1971; *Isacks and Barazangi*, 1977]. Studies of the physical processes that govern the style of subduction have compared individual subduction zones to identify the key parameters [e.g., *Jarrard*, 1986]. Unfortunately, as in the case of the dip of the subduction zone, this procedure does not always provide satisfactory results [*Jarrard*, 1986]. This might be due to the assumption that the observed present-day geometry of the slabs is the result of a steady state process. Some studies, however, indicate substantial time behavior of the evolution of subducted slabs [e.g., *Tao and O'Connell*, 1993], and the present configuration represents only a snapshot of the mantle flow.

Another possible procedure to address the physics of subduction is the construction of a model where the influence of different parameters can be tested and compared with observations. This can be achieved with either laboratory or numerical experiments; these two approaches are complementary. While laboratory models give a direct representation of the physical processes and allow the simulation of complex rheologies in three dimensions, numerical experiments are easier to study and replicate quantitatively. In this paper we discuss the results of both approaches to modeling the formation and evolution of slabs in the upper mantle. By comparing the two models we are able to identify and characterize simple yet important physical effects which govern the style of subduction. We test the following parameters: the velocity of convergence [e.g., *Luyendyk*, 1970; *Tovish and Schubert*, 1978; *Cross and Pilger*, 1982; *Furlong et al.*, 1982], the age of the oceanic lithosphere at the subduction zone [e.g., *Stevenson and*

[1]Permanently at Dipartimento di Science Geologiche, Universitá di Roma Tre, Rome, Italy.

Paper number 1999JB900140.
0148-0227/99/1999JB900140$09.00

Turner, 1972; *Molnar and Atwater*, 1978; *Uyeda and Kanamori*, 1979; *Cross and Pilger*, 1982; *Sacks*, 1983], here expressed as the density contrast between oceanic plate and upper mantle (compare the age-density diagrams of *Oxburgh and Turcotte* [1976], *Sacks* [1983], *Davies* [1992], and *Cloos* [1993]), and the viscosity contrast between the oceanic plate and the upper mantle. As a function of these parameters, we are able to model slab trajectories in a fluid upper mantle and to observe trench migration at the surface. We analyze the state of stress in the slab, and the overriding plate, the velocity and the dip of the slab and the mode of trench migration that result from the force equilibrium.

Subduction is similar in the two model approaches: it initiates slowly as a gravitational instability and becomes more pronounced as dense material sinks into the mantle. The speed of the downwelling increases roughly exponentially when the slab pull has overcome the resisting forces until the slab reaches the 670-km discontinuity in a time span of tens of millions of years. While the convergence velocity and the negative buoyancy of the oceanic plate represent the main driving forces in the system, the viscous drag in the oceanic plate as it bends turns out to be the major resisting one. This dynamical competition exerts the major control on the style of subduction in the upper mantle and can be characterized by the buoyancy number F. We start by presenting the model assumptions, techniques, and results of numerical and laboratory experiments and subsequently discuss the relevance of the governing physics for subduction in nature.

2. Model Definition: Assumptions and Boundary Conditions

Our experiments are set up in the following framework:

1. Following a design adopted by previous authors [e.g., *Jacoby and Schmeling*, 1981; *Kincaid and Olson*, 1987; *Gurnis and Hager*, 1988; *Tao and O'Connell*, 1992; *Zhong and Gurnis*, 1995; *Gouillou-Frottier et al.*, 1995; *Griffiths et al.*, 1995; *Faccenna et al.*, 1996], the experimental setting and the materials have been chosen to model a viscous slab. This rheology is an appropriate overall description since it has been supposed that lithosphere subjected to stress over geological timescales acts as a fluid of some sort. In fact, with an elastic lithosphere it is not possible to predict the shape of most of the Wadati-Benioff zones [*Bevis*, 1986], their strain rate [*Bevis*, 1988], and the highly curved subduction zones observed in some island arcs like the Marianas [*Hsui*, 1988]. Furthermore, slabs exhibit significant deep in-plane lateral deformation at depth [*Giardini and Woodhouse*, 1984] and appear to be folded at the transition zone [e.g., *van der Hilst et al.*, 1991], suggesting that the sinking lithosphere behaves similar to a viscous fluid [*Tao and O'Connell*, 1992].

In addition, the plates have been modeled using a viscosity which is constant both laterally and with depth. Hence the plate viscosity represents an average, effective value for the different parts of the lithosphere. Analytic results demonstrate that the formation of an instability is not significantly modified by the approximation of depth independence [*Martinod and Davy*, 1992]. Since the viscosity is homogeneous laterally, however, our statements about the importance of plate viscosities refer mainly to the regions involved in the subduction process, that is, the plate margin [e.g., *Jacoby and Schmeling*, 1981]. We furthermore use a Newtonian rheology, whereas laboratory data indicate that the upper mantle deforms obeying a power law with a stress exponent ranging between 1 and 3 [e.g., *Brace and Kohlstedt*, 1980]. In the discussion we will emphasize that this second approximation supports our arguments on time dependence.

2. Horizontal tectonic stresses from the combined effect of ridge push, basal drag under the oceanic plate, resistance to motion of the continental roots, and plate reorganization have been modeled by an oceanic plate which advances at a constant rate toward a fixed overriding plate. The upper plate is lighter and more resistant than the subducting one in order to simulate a craton-like region (Figure 1).

3. Previous experiments indicated that the presence of a preexisting fault or weak zone fixed in space exerts a strong control on the shape of the slab [*Zhong and Gurnis*, 1995; *King and Ita*, 1995; *Hassani et al.*, 1997] and on its velocity [*King and Hager*, 1990]. In our model, deformation is localized at a passive margin without the presence of a weak zone to avoid the a priori definition of the slab trajectory. Once subduction starts, the shape and the position of the converging margin evolve dynamically self-consistent under the prescribed boundary conditions.

4. We do not consider the effect of temperature or phase changes during the subduction process. As in previous models, this approximation has been adopted since our analysis is restricted to slab formation and evolution in the upper mantle where the subduction zone preserves its thermal field to first-order [*Wortel*, 1982]. Further, the numerical experiments have been constructed to be directly comparable to the laboratory ones, and it is one of our main points that first-order observations of subduction in nature can be explained by a Stokes flow model.

5. We assume a mantle with no trench-relative motion as a reference frame, realized by a fixed left sidewall in the experiments. Flow is then only produced by the relative plate motion, and we do not consider the effect of global [e.g., *Ricard et al.*, 1991] or local background mantle flow [e.g., *Russo and Silver*, 1994] that is not directly related to subduction.

On the basis of these assumptions our experiments are scaled to the Earth considering the Navier-Stokes equation for an incompressible fluid in the infinite Prandtl number and Boussinesq approximations. The resulting formula is Stokes' equation with a driving term due to density perturbations $\Delta\rho$:

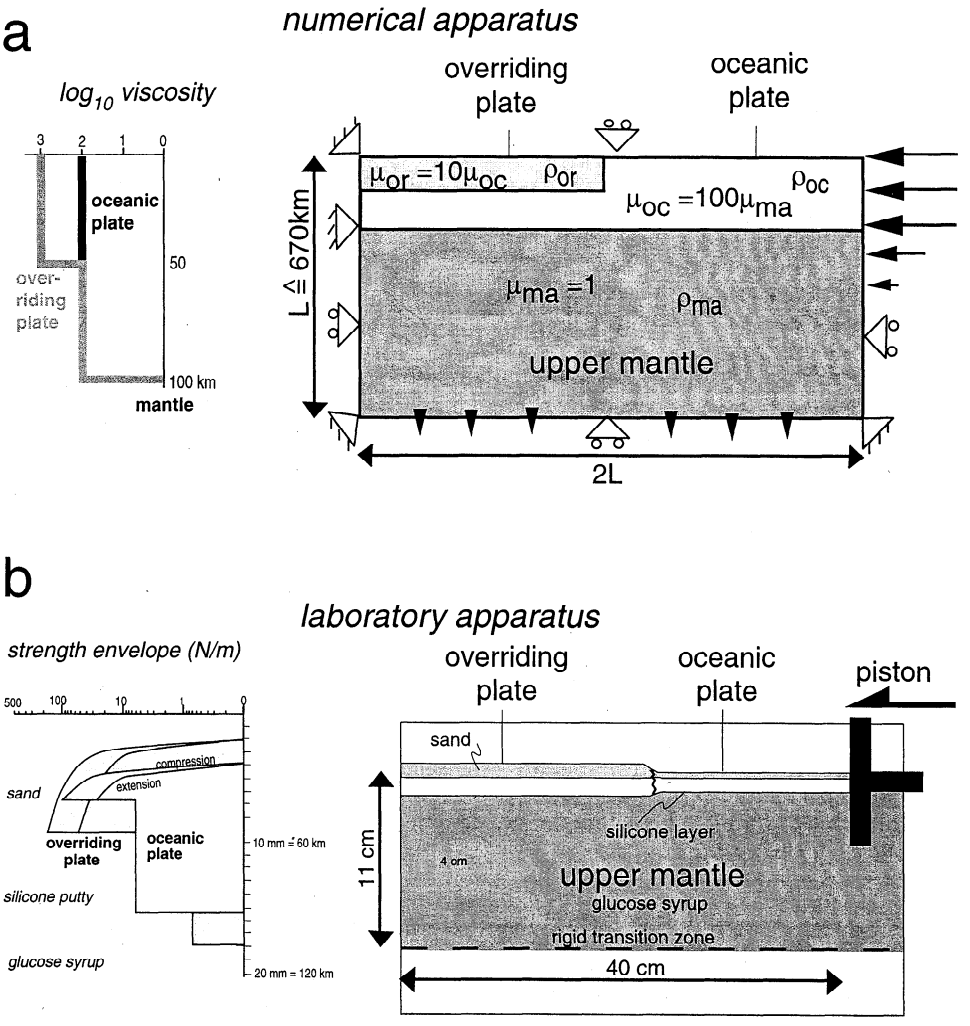

Figure 1. (a) Numerical and (b) experimental setups, boundary conditions and corresponding viscosity and yield strength envelopes of the lithospheric material used in the experiments. The laboratory strength envelopes have been calculated using a Mohr-Coulomb criterion for the sand layer and a creep law for the silicone layer [see *Davy and Cobbold*, 1991; *Faccenna et al.*, 1999b]. In particular, the latter has been estimated by multiplying the measured silicone putty viscosity with the velocity of convergence and dividing it by the thickness of the silicone layer (Table 2).

$$-\nabla p_d + \mu \nabla^2 \mathbf{u} - g\Delta\rho \mathbf{e}_z = 0. \quad (1)$$

Here the gravitational acceleration g is taken in z direction with unit vector $\mathbf{e}_z$, p_d is the dynamic pressure, $\mathbf{u}$ is the velocity, and μ is the dynamic viscosity. If we define a characteristic length L, velocity U, and density difference $\Delta\rho_0$, the pressure can be expressed as $p_c = \mu U/L$, the timescale is given by $t_c = L/U$, and the nondimensionalized version of (1) is

$$-\nabla \tilde{p}_d + \nabla^2 \bar{\mathbf{u}} - F\Delta\tilde{\rho}\mathbf{e}_z = 0. \quad (2)$$

Equation (3) introduces the buoyancy number F [e.g., *Houseman and Gubbins*, 1997]

$$F = \frac{L^2 g \Delta\rho_0}{\mu U} \quad (3)$$

which represents the ratio of the driving buoyant to the resisting viscous forces. (F can be transformed to the thermal Rayleigh number with $\Delta\rho = \rho_0 \alpha \Delta T$ and $U = \kappa/L$, where α and κ are the thermal expansion and diffusion coefficients, respectively.) For the Stokes flow problem, the appropriate scaling for U is $U \propto \Delta\rho R^2 g/\mu$, and the buoyancy number reduces to the length scale ratio L^2/R^2. As demonstrated in section 4.2, the characteristic U for our models is the velocity of convergence, u_r, while the governing viscosity μ is that of the oceanic lithosphere and L is the domain height corresponding to the upper mantle. Taking characteristic numbers for the Earth as those given in Table 1, the buoyancy number turns out to be ~14.

3. Model Setup

3.1. Numerical Experiments

We use the two-dimensional, Cartesian finite element code for incompressible convection ConMan by *King et al.* [1990]. A material field that corresponds to the

Table 1. Material Constants and Buoyancy Number for Earth, Numerical and Laboratory Reference Model

Nature	Numerical Reference Model (nondimensionalized units)	Laboratory Reference Model (7)
$\mu_{ma} = 2.5 \times 10^{20}$ Pa s	$\mu_{ma} = 0.1$	$\mu_{ma} \approx 50$ Pa s
$\mu_{oc} = 2.5 \times 10^{22}$ Pa s	$\mu_{oc} = 10$	$\bar{\mu}_{oc}^{eff} \approx 7 \times 10^5$ Pa s
		$\mu_{oc}^{sl} \approx 7 \times 10^4$ Pa s
$\mu_{or} = 2.5 \times 10^{23}$ Pa s	$\mu_{or} = 10\mu_{oc}$	$\mu_{or} \approx 10^4$ Pa s
$L = L = 6.7 \times 10^5$ m	$L = 1$	$L = 1.1 \times 10^{-1}$ m
$g = 9.81$ m/s^2		$g = 9.81$ m/s^2
$\rho_{oc} = 3300$ kg/m^3	$\rho_0 = 1$	$\rho_{oc} = 1474$ kg/m^3
$\rho_{or}^{upper} = 2800$ kg/m^3		$\rho_{or} = 1282$ kg/m^3
$\rho_{or}^{lower} = 3300$ kg/m^3	$g\Delta\rho_{ma}^{oc} = 70$	
$\rho_{ma} = 3220$ kg/m^3		$\rho_{ma} = 1410$ kg/m^3
$\Delta\rho_{ma}^{oc} = 80$ kg/m^3		$\Delta\rho_{ma}^{oc} = 64$ kg/m^3
$u_r = 10^{-9}$ m/s ≈ 3.2 cm/yr	$u_r = 0.5$	$u_r = 6.9 \times 10^{-7}$ m/s
$p_c = \sigma_c = \mu_{oc} u_r / L \approx 37.3$ MPa	$\sigma_c = 50$	$\sigma_c \approx 4.2$ Pa
$\Phi_c = \sigma_c^2 / \mu_{oc} \approx 56$ nW/m^3	$\Phi_c = 250$	
$t_c = L/u_r \approx 21$ Myr	$t_c = 2$	$t_c = 46$ hours
	$1 \equiv 10.5$ Myr	$1h \equiv 0.5$ Myr
$F = \frac{L^2 g \Delta\rho_{ma}^{oc}}{\mu_{oc} u_r} \approx 14.1$	$F = 14$	$F \approx 15.7$

Parameters are μ, dynamic viscosity; L, domain height; g, gravitational acceleration; ρ, density; u_r, velocity of convergence; p, pressure; σ, stress; Φ, viscous dissipation; t, time; and F, buoyancy number. Abbreviations are c, characteristic; oc, oceanic plate; ma, mantle; or, overriding plate; sl, silica layer, and eff, effective.

density anomalies is advected with a zero diffusivity, while only two material isolines (indicated in Figures 2, 4, and 5) are utilized to track the boundary between plates. On this basis we assign a constant Newtonian viscosity within each different material. As discussed by *Lenardic and Kaula* [1993], the numerical method we use has shortcomings for strong viscosity contrasts and an unavoidable numerical diffusion is introduced. However, since we are only interested in simple convection processes without multiple overturns, these inaccuracies play a subordinate role in our models, and in general, the viscosity and material field match well. We tested the effect of small inaccuracies, and they did not influence the flow field by $> 2\%$. The geometry of our computational domain is rectangular with 1 by 2 aspect ratio to simulate an upper mantle region of dimensions 670 km by 1340 km, and the experimental design and model parameters are summarized in Figure 1a and Table 1. A regularly spaced finite element mesh of 128×128 second-order elements is applied for all models shown here. We estimate that our results are accurate at a relative error of $< 5\%$ total with respect to mesh refinement from 64×64 to 256×256 elements and other inaccuracies such as those mentioned above.

The oceanic lithosphere is driven from the right side of the box at a prescribed horizontal convergence velocity u_r toward a fixed overriding plate which is characterized by a more viscous (10 times) and less dense upper crustal layer. The boundary conditions on the upper boundary and the lower parts of the side boundaries are free slip, while the lower boundary has a prescribed vertical outflow to enforce mass conservation (too small to show up in the flow field plots) and no constraint on the horizontal velocity. We examined the influence of different boundary conditions, such as no slip instead of free slip along the lower sides of the box and found no substantial differences in model behavior (see section 4.4). The ratio between oceanic and mantle viscosity (μ_{oc}/μ_{ma}) and the density contrasts between the plates are varied for different experiments.

3.2. Laboratory Experiments

Laboratory models have a layered setup adopted by previous authors [*Davy and Cobbold*, 1991; *Martinod and Davy*, 1994; *Faccenna et al.*, 1999b, and references therein] to simulate the stratified lithospheric rheological profile [e.g., *Ranalli and Murphy*, 1986], while similarity criteria with respect to the Earth are fulfilled with stress scaled for gravity [*Davy and Cobbold*, 1991] (Figure 1b). The model lithosphere consists of sand mixed with ethyl cellulose representing the brittle behavior of the upper crust and silicone putty modeling the viscous rheology of the lower crust and mantle lithosphere; the brittle-ductile layers rest on glucose syrup mimicking the asthenosphere.

The mixture of sand and ethyl cellulose is a cohesionless Mohr-Coulomb material with a mean frictional angle of 30° and a density ranging from 1300 to 1500 kg/m^3. For the strain rates that are characteristic

for our experiments the silicone putty is a Newtonian fluid with a viscosity of 10^4 to 10^5 Pa s at room temperature [*Weijermars*, 1992; *Davy and Cobbold*, 1991], while we can vary its density by changing the fraction of inert fillers (galena powder). The glucose syrup is a Newtonian low-viscosity (~10 to 100 Pa s) and high-density (1410 kg/m^3) fluid. As in other models [e.g., *Kincaid and Olson*, 1987], the plate/slab viscosity is ~1000 times the mantle viscosity to obtain a "plate-like" behavior, while our experiments are conducted at constant room temperature.

At an analogue depth of 670 km, we imposed a rigid surface to simulate a deep transition zone where the slab can be anchored. Two different plates are prepared (Figure 1b). One has a lower mean bulk density than the glucose syrup, simulating an upper overriding plate; the second, subducting "oceanic" plate is denser than the glucose syrup, with varying densities in different models to simulate its agedependence (Table 2). Details on the similarity criteria, material rheology, and experimental technique are given by *Davy and Cobbold* [1991] and *Faccenna et al.* [1996, 1999b]. Models are constructed and deformed inside a rectangular Plexiglas tank (dimensions are 47 cm long, 25 cm high and 35 cm wide; Figure 1b). A compressional stress regime is achieved by displacing a rigid piston at constant velocity perpendicular to the plate margin. The piston is confined to the upper middle part of the tank, and the glucose syrup is free to move underneath.

For each model we estimate the buoyancy number F. However, the comparison between the laboratory experiments which have a layered, complicated rheology (Figure 1b) and the purely viscous numerical models (Figure 1a) is not straightforward and is based on a scaling argument described in section 4.3.

Table 2. Experimental Parameters Used for the Laboratory Models.

	h, mm	ρ, kg/m^3	ρ_{avg},[a] kg/m^3	μ, 10^4 Pa s
	Experiment 9			
Oceanic plate			1455	
Silicone layer[b]	9	1440		7
Sand layer	3	1500		
Overriding plate			1282	
Silicone layer[b]	10	1270		3
Sand layer	7	1300		
Velocity u_r, 10^{-7} m/s	6.9			
Buoyancy no. F	11			
	Experiment 7			
Oceanic plate			1474	
Silicone layer[b]	9	1465		7
Sand layer	3	1500		
Overriding plate			1282	
Silicone layer[b]	10	1270		3
Sand layer	7	1300		
Velocity u_r, 10^{-7} m/s	6.9			
Buoyancy no. F	15.7			
	Experiment 15			
Oceanic plate			1485	
Silicone layer[b]	9	1480		7
Sand layer	3	1500		
Overriding plate			1282	
Silicone layer[b]	10	1270		3
Sand layer	7	1300		
Velocity u_r, 10^{-7} m/s	6.9[c]			
Buoyancy no. F	18.4[c]			

The underlying, glucose mantle layer has a density of 1410 kg/m^3 and viscosity of ~50 Pa s, h is the thickness of the layer.

[a] $\Delta\rho_{ma}^{oc}$ = 45 kg/m^3 for experiment 9, 64 kg/m^3 for experiment 7, and 75 kg/m^3 for experiment 15.

[b] Values are averaged for upper and lower silicone layer; viscosity is measured at room temperature.

[c] During the first 20 hours after which $u_r = 0$.

4. Results

4.1. Effect of the Buoyancy Number F

We will present three numerical and two laboratory experiments to explain how the style of subduction depends upon F. The first, numerical "reference" model with $F = 14$ is illustrated in Figure 2 at four time steps at 0, 21, 42, and 63 Myr. During the first stage of deformation the oceanic plate thickens, and a large instability forms at the boundary with the stiff overriding plate, progressively growing in depth while reducing its lateral extent (Figures 2a and 2b). Both the stiff overriding and the oceanic plate are initially subjected to mainly horizontal compression. After the formation stage the instability develops the shape of a slab sinking into the mantle at a shallow angle. The stress state in the subducting oceanic plate is basically downdip extension from 26 Myr on and at a maximum at the trench, while the deformation within the overriding plate has changed from in-plane compression to extension (Figure 2c). The downward velocity of the oceanic plate increases further until 40 Myr and leads to a rapid growth in the depth of the subduction zone with time. The maximum downward velocity of the slab tip is 72% of the convergence velocity u_r and reached shortly before the slab is slowed down by the effect of the lower boundary (Figure 3a). Afterward, the slab reaches the lower part of the box (47 Myr), decreases its speed steeply as the tip thickens, and experiences compression since it cannot flow at the same rate through the lower boundary (Figures 2d and 3a). As a consequence, the stress changes from in-plane compression to in-plane extension roughly at half depth. The closed bottom boundary can be considered as an end-member case of maximum slab impediment for Earth. Contrasting models with a free bottom boundary (not presented here) show a similar style of subduction, but the slab undergoes only downdip tension, and the initial subduction velocity is higher by ~10 to 15%.

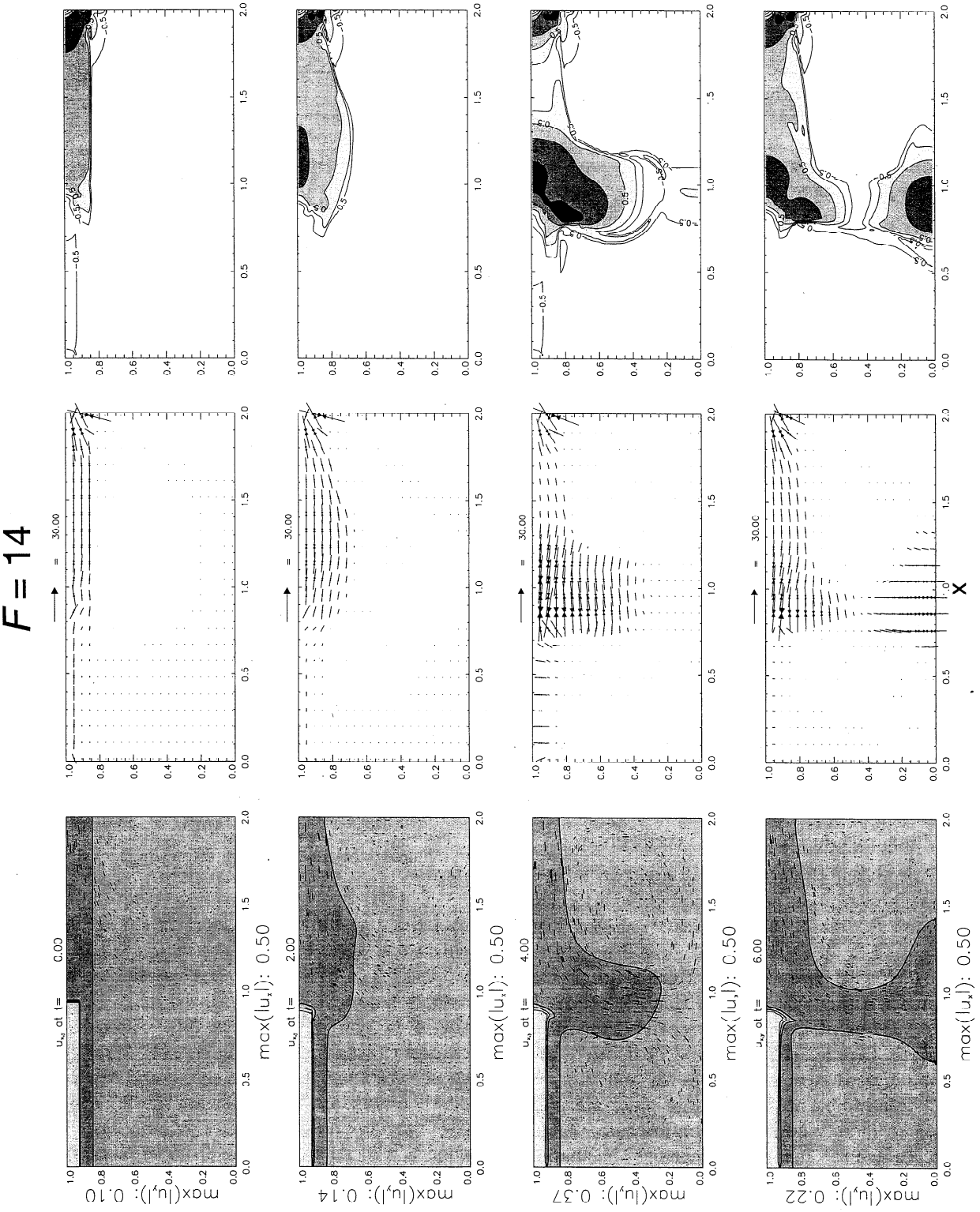
F = 14
a
b
c
d
x
max(|u_y|): 0.10
max(|u_y|): 0.14
max(|u_y|): 0.37
max(|u_y|): 0.22
max(|u_x|): 0.50

The second numerical experiment in Figure 4 has a buoyancy number that is increased twofold ($F = 28$) compared to the reference model. The first stage of deformation is similar to the $F = 14$ model, but now the velocity of subduction is greater, while the maximum downward slab tip velocity (about $1.9u_r$) is again reached shortly before the slab is slowed down by the lower boundary (Figure 3a). In this experiment the trench migrates toward the ocean at half the velocity of subduction (Figure 3b), and the upper plate is in extension during the entire experiment. Moreover, a larger amount of upper plate material, as compared to the reference model, is dragged down and ablated into the subduction zone. The slab reaches the lower boundary after 34 Myr (Figure 4c) causing a decrease in the rate of subduction and of trench migration (Figures 3a, 3b).

Figure 5 shows the evolution of the third numerical experiment where the buoyancy forces are decreased twofold ($F = 7$) compared to the reference model. The velocity of subduction is slower for this model, reaching a value of <63% of u_r (Figure 3a). The slab is also thicker and sinks at an initially lower dipping angle into the mantle. This causes a migration of the trench at constant rate toward the overriding plate (Figure 3b), which is subjected to compression, particularly during the first stages of the experiment (Figure 5). Further, a smaller amount of upper plate material than in the reference model is ablated and subducted. The slab reaches the bottom of the box after 60 Myr. When we decreased F further, subduction was slowed down ultimately and ceased when the tectonic style was transformed into a underthrusting regime at $F \approx 2.5$.

To compare these findings with laboratory models, we choose two out of a total of 30. In the laboratory reference experiment 7 shown in Figure 6 the density contrast between the oceanic plate and the mantle is 64 kg/m^3, and $F = 15.7$ with $\bar{\mu}_{oc}^{eff} \approx 7 \times 10^5$ Pa s. Subduction develops slowly from an instability at the plate boundary, and it takes 20 hours (10 Myr) until a 4 cm long slab sinks into the mantle [see also *Faccenna et al.*, 1996, 1999b]. The subduction speed then increases to roughly the convergence velocity after 30 hours; at this stage (Figures 6 and 7a) the slab has also attained a steeper dip (Figure 7a inset). The thinning observed in its middle portion suggests that strong tensional forces are pulling the slab down (Figure 6a). During the whole experiment the overriding plate is not subjected to substantial compression or extension, and the trench is essentially stationary. Its apparent migration toward the continent is due to an erosion of both upper plate layers into the subduction zone, while the amount of eroded material is roughly constant and ~30% of the total amount of subducted material. Hence the shortening produced by the advancing piston is entirely transmitted to the subduction zone (Figure 7b). After ~45 hours (Figure 6b) the slab reaches and anchors at the rigid transition zone, causing compression and folding at its tip. The description of the deformation at depth is beyond the scope of this paper, and further experiments with a more realistic viscosity increase are needed. For our experiments it is sufficient that the slab tip is anchored at depth. We then stop the piston to observe that the hinge of the slab starts to roll backward with respect to its anchored tip; the slab progressively rotates and decreases its dip to 60°, producing extension of the overriding plate (Figure 6c, 7b, and 7a inset). We note that both numerical and laboratory reference models are alike in terms of the apparent deformation state, the time dependence of subduction speed, and the absence of trench migration (compare Figures 3a and 3b with Figures 7a and 7b).

A decrease in F as is in the numerical $F = 7$ model of Figure 5 can be illustrated by the laboratory experiment 9 shown in Figure 8 where the density contrast between ocean and mantle is 45 kg/m^3 and $F = 11$. Initial deformation is followed by underthrusting of the oceanic under the overriding plate after 13 hours (6 Myr) and a 1 cm long slab sinks at a low angle (< 20°) into the mantle (Figures 7a inset and 8b). After 10 cm of compression (Figure 8d) the slab has grown to 3- to 4-cm length, and its dip is ~30°. Since the velocity of subduction is lower than the velocity of convergence, the excess compression causes internal bulk shortening and thickening of the slab (Figure 7b). As in the numerical experiment with low F, we now observe trench migration toward the upper plate which is thus subjected to compression. The rate of subduction is constant and mainly controlled by the advance of the piston (Figure 7a). At the same time, the slab dip progressively increases under the weight of the subducted material (Figures 8d and 7d). The experiment is halted after 54 hours when a 4- to 5-cm long, 60° dipping slab sinks into the mantle. The fraction of material from the upper plate which gets dragged down into the subduction zone is ~15% of the total amount of subducted material.

Figure 2. (left) Material contour lines and flow field, (middle) orientation and magnitude of the principal compressional stress axis, and (right) decadic logarithm of the viscous dissipation log(Φ) for the numerical reference experiment with $F = 14$. All quantities are given in nondimensional units. The time steps are (a) 0, (b) 21, (c) 42, and (d) 63 Myr. Vectors scale with the magnitude of the local field, and the velocity of convergence that we prescribe on the right-hand side is 0.5, corresponding to 3.2 cm/yr in nature. Stresses of magnitude 30 as indicated by the reference vector above the center plots correspond to 22.5 MPa. Φ for incompressible 2-D flow is calculated by $(\sigma_{xx}^2 + \sigma_{xz}^2)/\mu$, and log($\Phi$) isolines are plotted from −0.5 to 2.0 in 0.5–intervals (see Table 1).

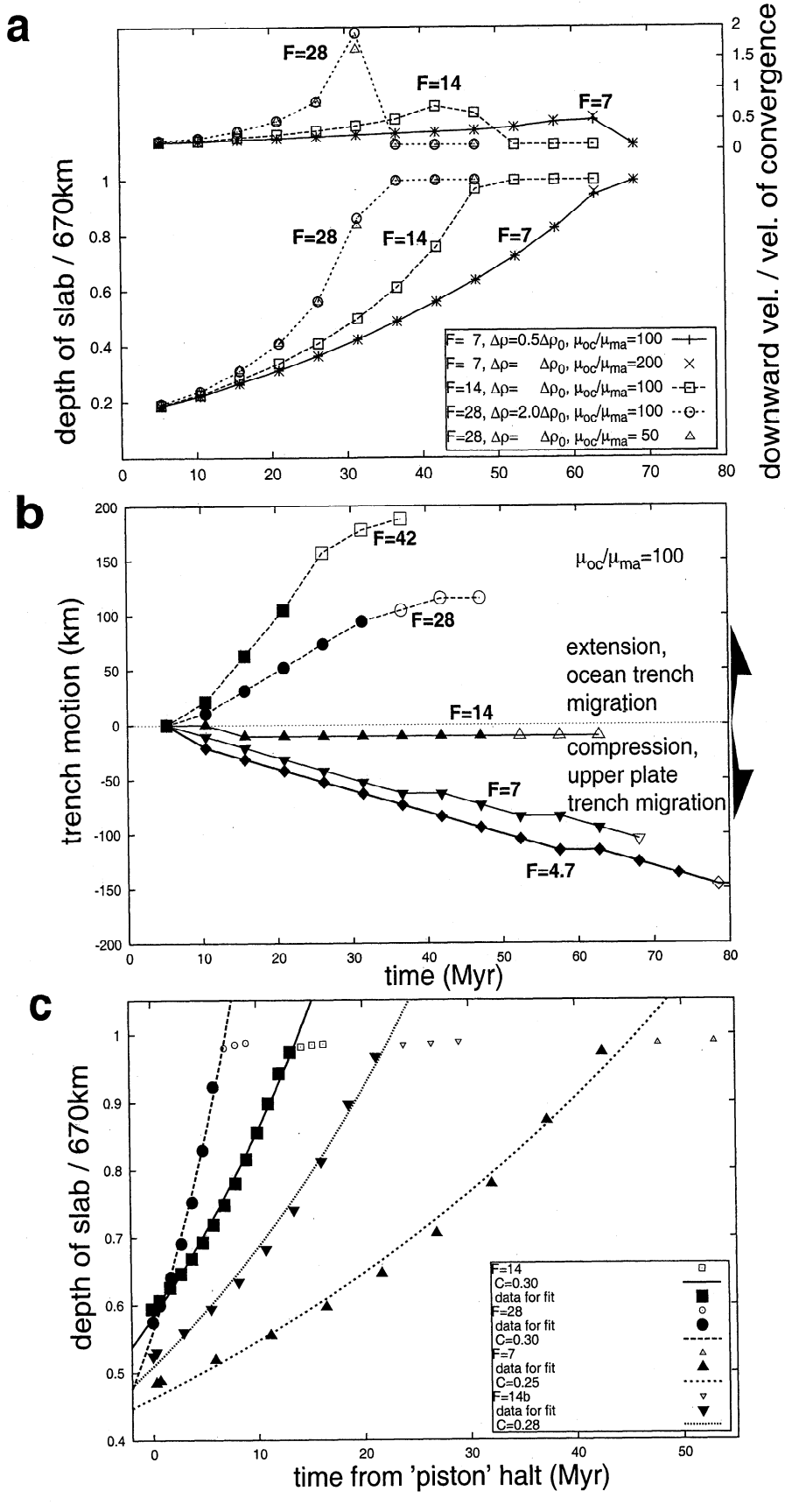
a
F=28
F=14
F=7
F=28
F=14
F=7
depth of slab / 670km
downward vel. / vel. of convergence
F= 7, Δρ=0.5Δρ0, μoc/μma=100
F= 7, Δρ= Δρ0, μoc/μma=200
F=14, Δρ= Δρ0, μoc/μma=100
F=28, Δρ=2.0Δρ0, μoc/μma=100
F=28, Δρ= Δρ0, μoc/μma= 50
b
F=42
F=28
μoc/μma=100
extension,
ocean trench
migration
F=14
compression,
upper plate
trench migration
F=7
F=4.7
trench motion (km)
time (Myr)
c
depth of slab / 670km
time from 'piston' halt (Myr)
F=14
C=0.30
data for fit
F=28
data for fit
C=0.30
F=7
data for fit
C=0.25
F=14b
data for fit
C=0.28

In summary, laboratory and numerical experiments indicate that the buoyancy number F controls the speed and the deformational style of subduction as well as the shape of the slab and the mode of trench migration. Different system behavior can be realized by varying the density contrasts of the plates.

4.2. Role of Viscosity, u_r and Relative Density Contrasts Between Plates

In the numerical models described in section 4.1, the value of F is changed by varying the absolute density contrasts, $g\Delta\rho_0$. However, experiments with the same corresponding values for F (7, 14, 28), which were done by changing the viscosity of the oceanic plate or the velocity of convergence but leaving $g\Delta\rho_0$ constant, give very similar results to those illustrated above (Figure 3a). This finding demonstrates that the parameters adopted in (3) represent the relevant controls on the style of model subduction and F is suited to be used as a similarity number. Thus increasing the density contrast corresponds to decreasing the viscosity and vice versa.

Further numerical experiments were conducted to investigate the role of the absolute and relative density contrasts between the layers by means of varying the density of the overriding plate and the ocean separately with respect to a fixed mantle density. It turns out that the density contrast between the oceanic plate and mantle (the slab pull) is the major control on the speed of subduction. The density difference between overriding plate and ocean (leading to a spreading tendency of the overriding plate) on the other hand plays a subordinate role, and its effect on the depth versus time curves as in Figure 3a is smaller by a factor of roughly 5.5. The density difference between these plates, however, has about the same effect on the rate of trench migration and the deformation state in the lithosphere as the mantle-ocean buoyancy contrast.

4.3. Free Subduction and Viscous Dissipation

As shown by the plots of the decadic logarithm of the viscous dissipation Φ on the right-hand side of Figures 2, 4, and 5, dissipation in the numerical models is most pronounced in the trench area, within the high-viscosity slab and on the right boundary. The latter is an artifact of our prescribed convergence velocity. Since the rheology is Newtonian, the deformation is rather broadly distributed with a significant concentration in the trench area. The maximum values of Φ are 20%, 50%, and 126% of the characteristic Φ_c of 56 nW/m^3 for $F = 7$, 14, and 28, respectively (Table 1). Since Φ_c is of the order of typical radiogenic rates of basalts [e.g., *Stacey*, 1992, p. 300], our Newtonian models do not predict excessive heat production due to shear heating. A viscous heating feedback mechanism between the rheology and the strain field can be expected to be more pronounced for a power law rheology [e.g., *van den Berg and Yuen*, 1997] so that we can not rule out this possibility here. We will, however, proceed to interpret our subduction models as controlled by viscous dissipation in the oceanic plate, more specifically by viscous bending of the slab.

To investigate the driving and resisting forces contributing to the balance as expressed by F further, the role of the slab pull and the viscous dissipation within the oceanic plate will now be studied with four numerical experiments lacking a prescribed convergence velocity. The "piston" push is used to initiate the subduction, but u_r is set zero afterward, and the system is left free to evolve. As in previous models, the length of the slab increases rapidly with time before it is slowed down by the lower boundary (Figure 3c). Furthermore, the trench moves toward the oceanic plate (rollback) after the piston is halted. We tested three models with the geometry shown in Figure 1a (density contrasts yielding $F = 7$, 14, and 28) and one model with a thicker oceanic plate and $F = 14$ (F calculated for the usual $u_r \neq 0$).

Figure 3. (a) Depth of the slab (bottom, depth defined by the lowest point of the isomaterial line used to mark the boundary between oceanic and mantle material in Figure 2) and downward velocity of the slab tip (top) versus time. We show data from numerical models: reference with $\Delta\rho = \Delta\rho_0$ and $\mu_{oc}/\mu_{ma} = 100$ ($F = 14$), two models with $\Delta\rho = 2\Delta\rho_0$ and $\mu_{oc}/\mu_{ma} = 100$, and $\Delta\rho = \Delta\rho_0$ and $\mu_{oc}/\mu_{ma} = 50$, respectively (both equating to $F = 28$); and finally two models with $\Delta\rho = 0.5\Delta\rho_0$ and $\mu_{oc}/\mu_{ma} = 100$, and $\Delta\rho = \Delta\rho_0$ and $\mu_{oc}/\mu_{ma} = 200$, respectively ($F = 7$). (b) Motion of the trench for $\mu_{oc}/\mu_{ma} = 100$ (defined by the boundary between upper and oceanic plate material) versus time for numerical models with buoyancy numbers of $F = 4.7$, 7, 14, 28, and 42. (End-member models with $F = 4.7$ and 42 are not discussed in the text.) Solid symbols change to open ones when $z > 0.97$. (c) Free subduction models; depth of the slab versus time after the velocity of convergence at the right boundary was set to zero following the initiation of subduction. Data from three models with the geometry shown in Figure 1 ($F = 7$, 14, and 28) and one with a thicker oceanic plate, indicated by "14b." The data points (solid symbols) which were used for a least squares fit of equation (4) (lines) are indicated together with the resulting values for the fitting constant C and the discarded data when the slab reached the bottom (small open symbols).

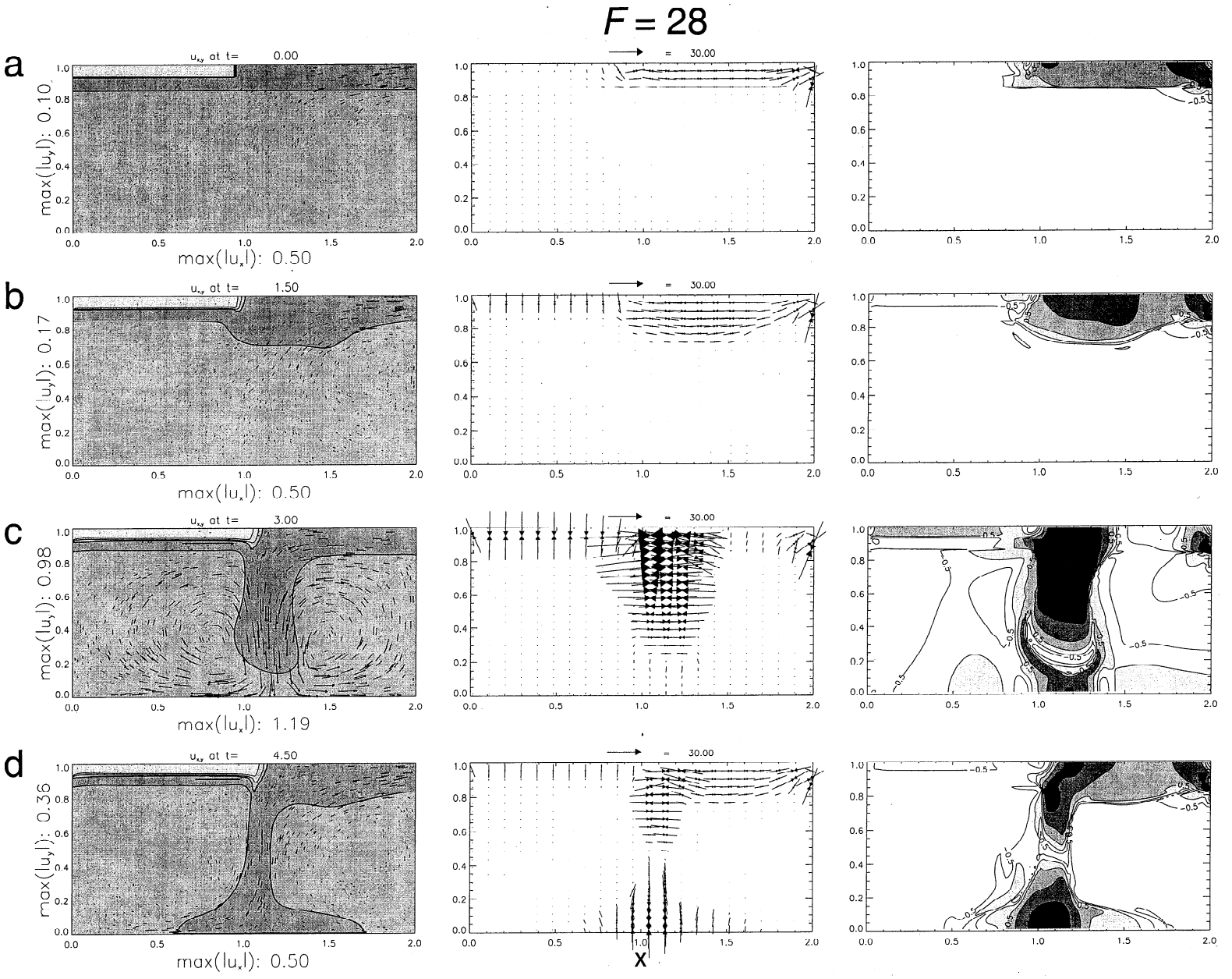

Figure 4. Evolution of numerical model $F = 28$; see Figure 2 explanation. Time steps are different since $F > 14$ implies a faster subduction and correspond to 0, 15.8, 31.5, and 47.3 Myr. The characteristic velocity and stress are the same as in Figure 2.

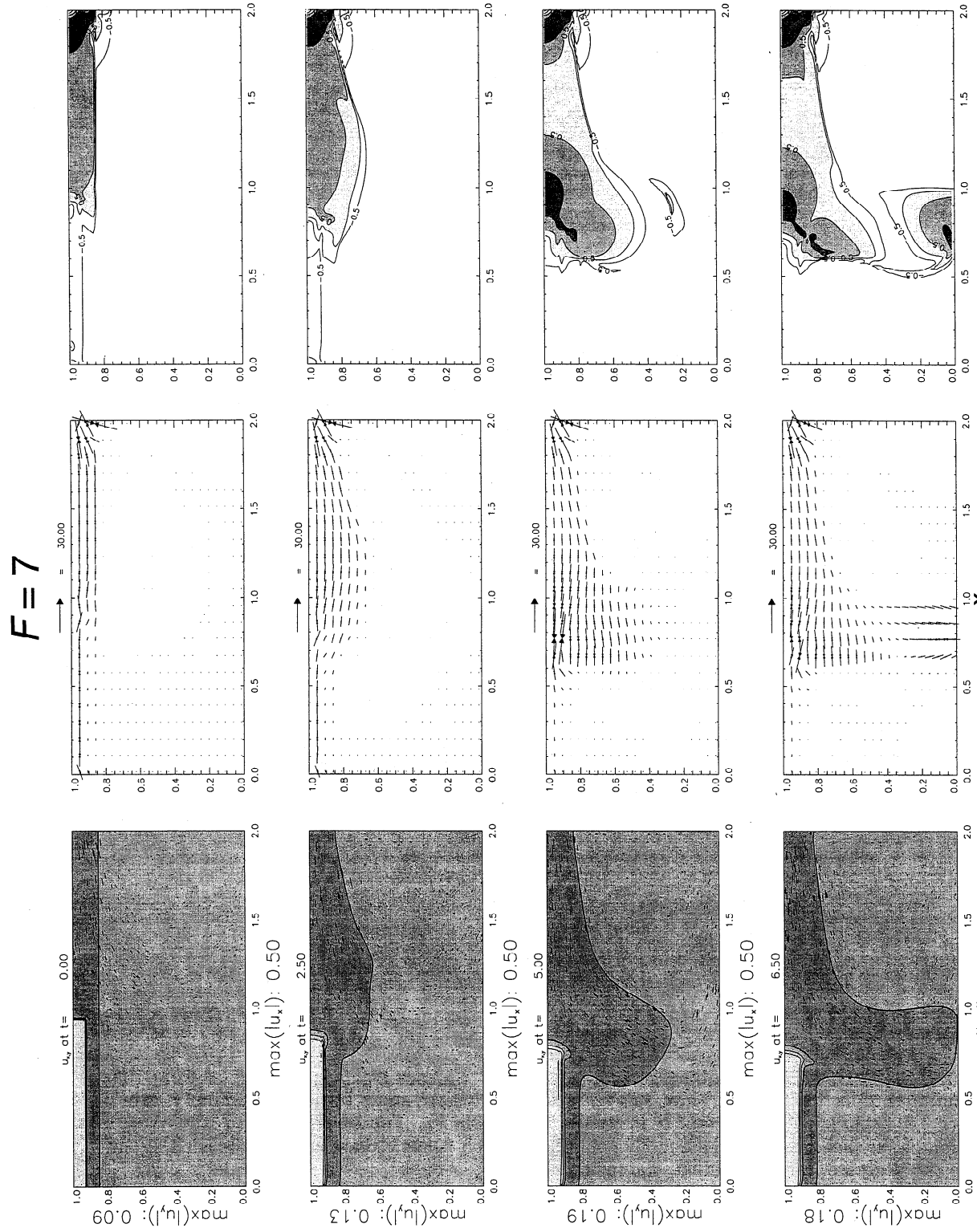

Figure 5. Evolution of numerical model $F = 7$; see Figure 2 explanation. Time steps are different since $F < 14$ implies a slower subduction and correspond to 0, 26.3, 52.2, and 68.3 Myr. The characteristic velocity and stress are the same as in Figure 2.

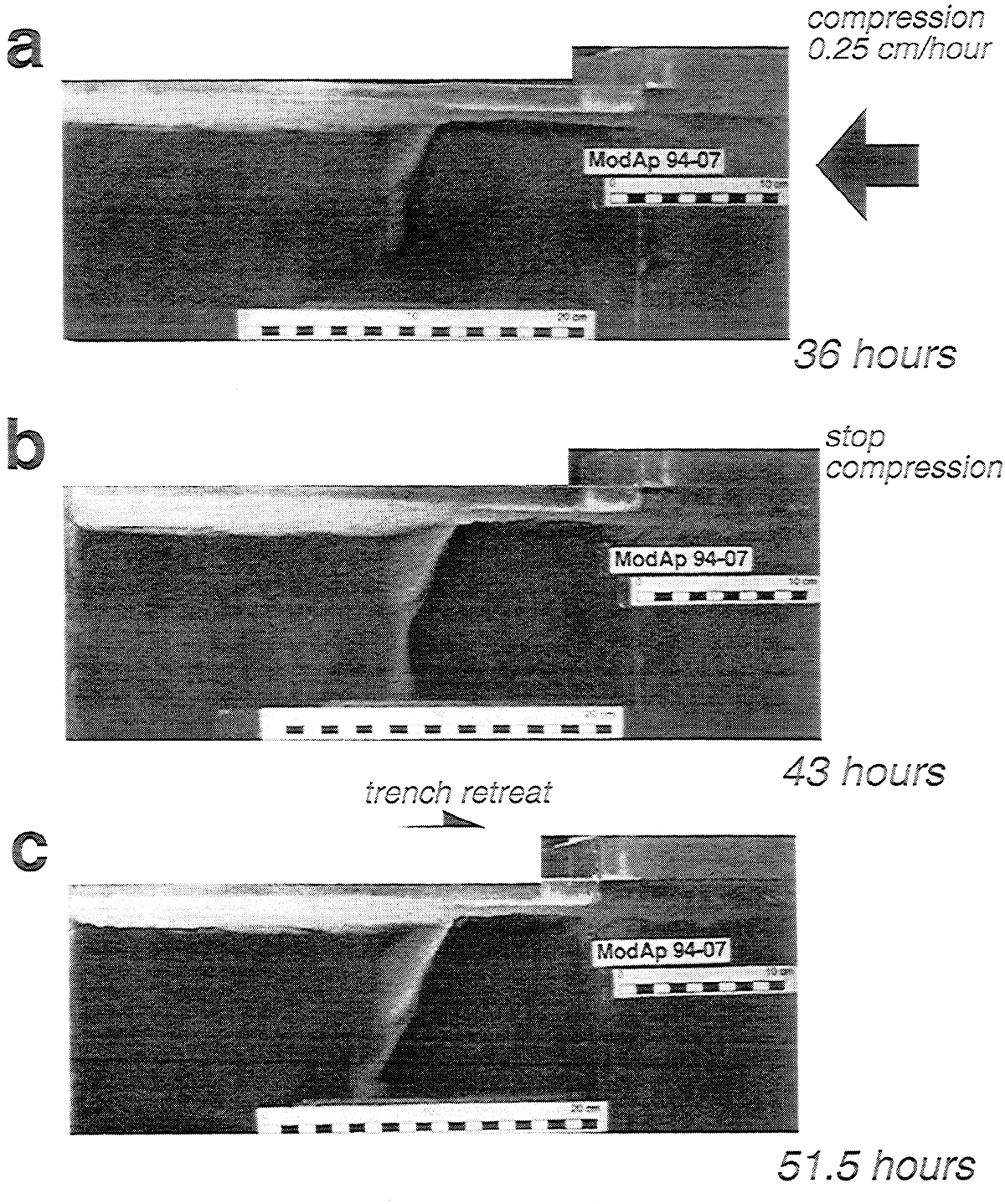

Figure 6. Three stages of subduction for laboratory reference experiment 7 ($F = 15.7$). The piston, acting on the oceanic plate, advances for the first 47 hours of deformation at a rate of 0.25 cm/h, equivalent to 3.2 cm/yr in nature (see Table 1). The arrow indicates the sense of motion of the piston, where the density contrast between oceanic plate and mantle is 64 kg/m^3. Note the decrease in the dip of the slab after anchoring at depth.

Following *Turcotte and Schubert* [1982] and *Conrad and Hager* [1997], the experimental data in Figure 3c can be fitted by calculating the viscous dissipation per unit length due to the bending of oceanic lithosphere which scales as $u^2\mu_{OC}R^3/r^3$. Here, u is the local subduction velocity at time t, R is the half width of the bending plate, and r is the radius of bending. If the balancing term at each moment is roughly equal to the potential energy dissipation due to the negative buoyancy of the already subducted slab of height H ($\propto \Delta\rho g H R u$), then $u(t) \approx dH(t)/dt$ yields

$$H(t) \propto H_0 \exp\left(C\frac{\Delta\rho g r^3}{\mu_{OC}R^2}t\right). \quad (4)$$

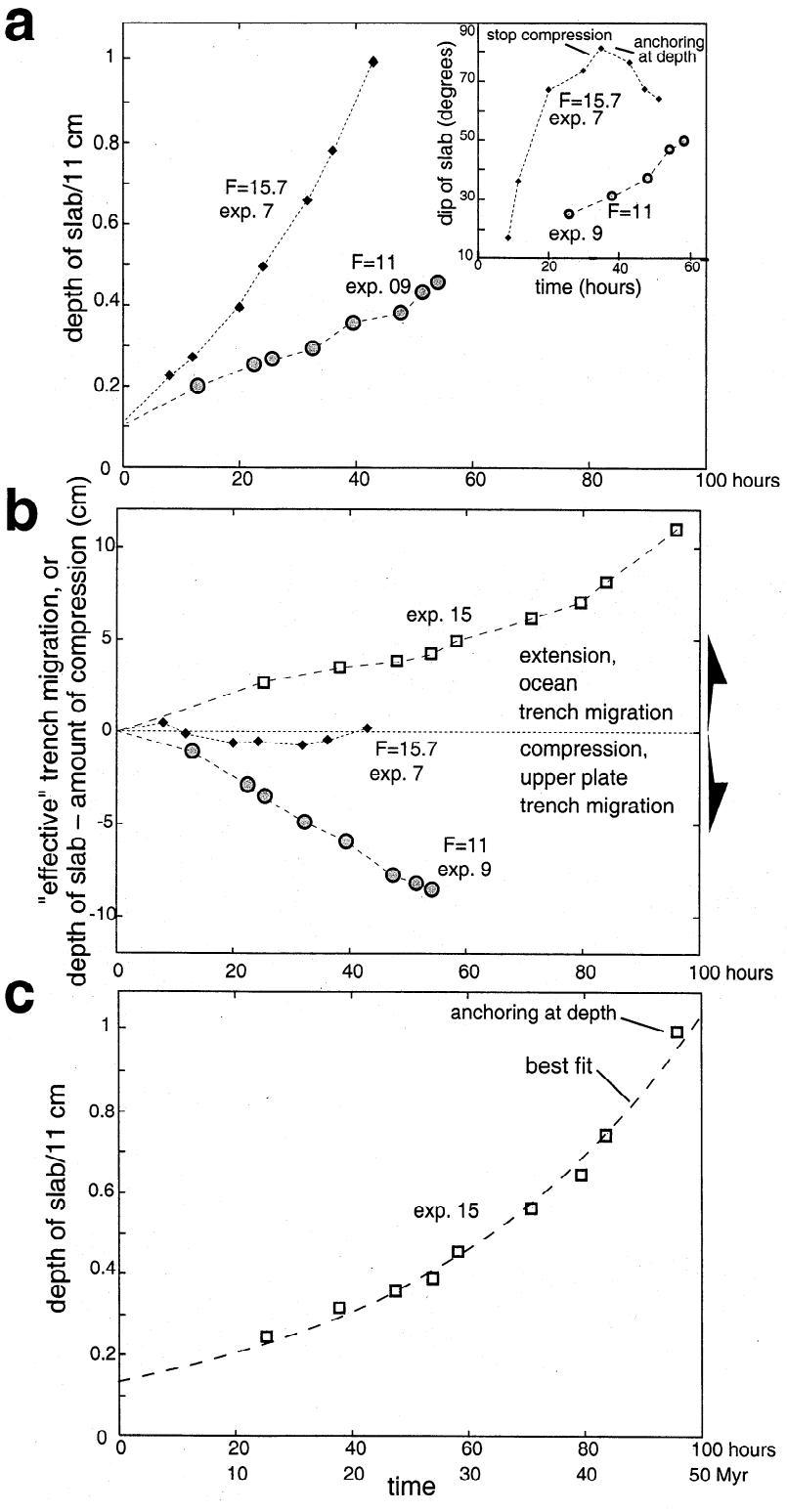

Figure 7. (a) Diagram illustrating the depth of the slab versus time for the laboratory reference model 7 with $F = 15.7$ and for experiment 9 with $F = 11$. Figure 7a inset is dip of the slab versus time for experiments 7 and 9. Note the decrease in subduction angle after anchoring at depth for experiment 7. (b) Effective trench motion, estimated by subtracting the amount of compression from the depth of the slab for laboratory experiments with $F = 15.7$, 11, and 18.4 for experiment 15, where the piston was stopped after 20 hours of compression. The effective trench motion is used to eliminate the effect of upper plate erosion from the data. (c) Free subduction model; depth of the slab versus time after the velocity of convergence was set to zero following the initiation of subduction. The best fit curve is used to estimate the effective viscosity of the experiment (7×10^5 Pa s for $C = 0.28$, $R = 6$ mm and $r = 9$ mm) from equation (4).

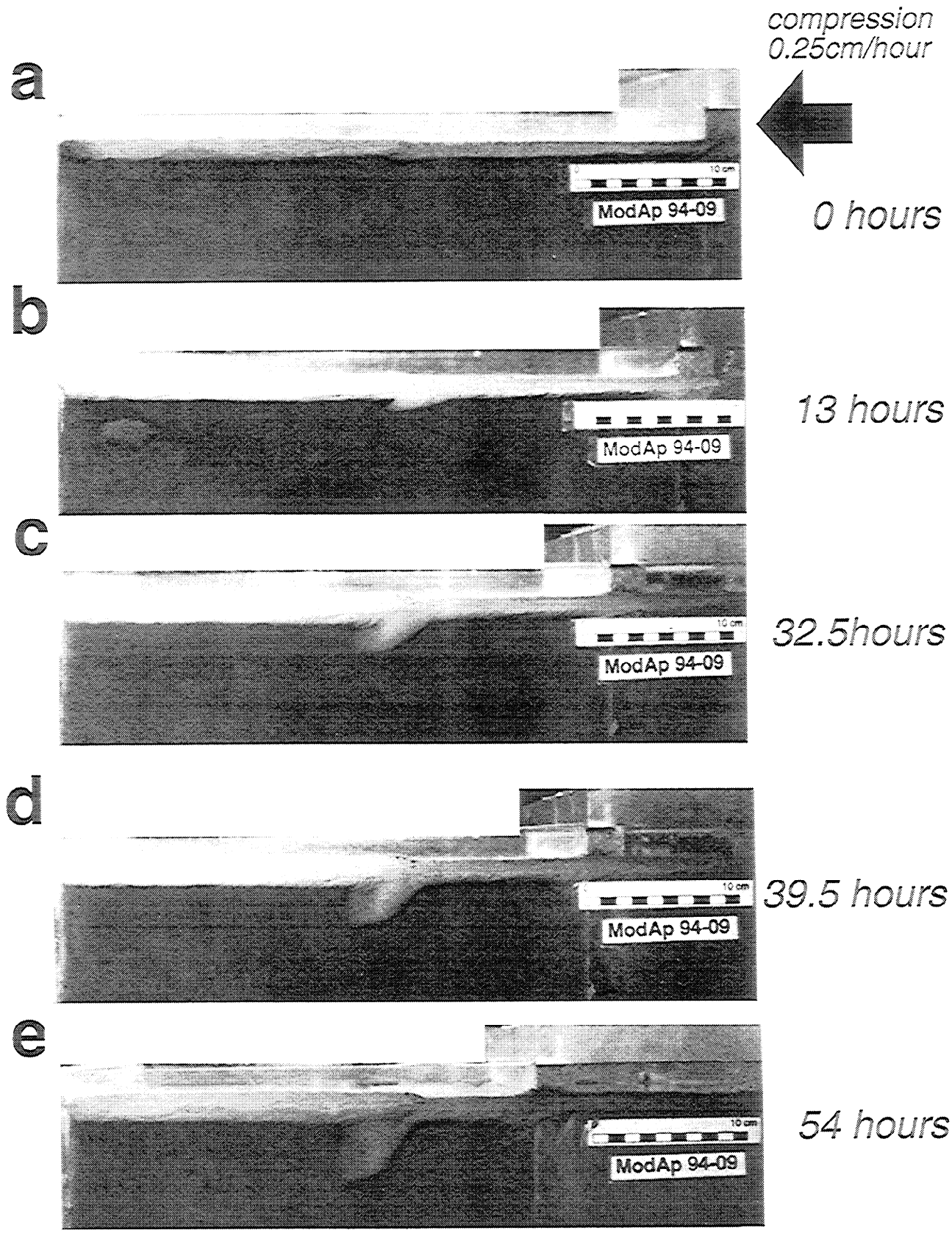

Figure 8. Five stages of the evolution of laboratory experiment 9 with $F = 11$ for a density contrast of 45 kg/m^3 between oceanic plate and mantle.

Here C is a fitting constant of order unity and H_0 is the initial driving instability. Equation (4) is clearly only a first-order estimate since we have assumed that only the bending of the oceanic plate and the gain in buoyancy forces are relevant, that R and r are constant during subduction (which they are not), and that the entrainment of upper plate lithosphere as well as the varying dip of the slab are not important. However, we determined the geometry parameter r^3/R^2 numerically by tracing a midslab stream line and measuring the minimum radius of curvature at each time step. A fit of the data could then be obtained by using the time average of the roughly linearly increasing geometry parameters for each experiment (Figure 3c). The values we obtain for C have remarkably small variations in the best fits from model to model, and we use the average, $C = 0.28$, to establish an empirical relation for $H(t)$ for "free" subduction. All our numerical data can thus be interpreted in a consistent way such that the most important resisting force is the viscous drag in the oceanic plate, more specifically in the trench region where the slab is bent.

In laboratory experiment 15 (not illustrated; see *Faccenna et al.* [1996]), the density contrast between ocean and mantle is 75 kg/m^3. Analogous to the numerical results above, we reanalyze the style of subduction for a system driven only by the weight of the slab after an initial piston advance (Figure 7c). During the free subduction process, the laboratory model also shows slab hinge rollback, causing a retreat of the trench toward the ocean and extension in the overriding plate (Figure 7b). We used the experimental data with the scaling relation, equation (4), to arrive at an average, first-order viscosity estimate for the multilayered laboratory system. Figure 7c shows that an exponential fit like (4) is suited for the free subduction data from the laboratory. Interpreting this fit quantitatively assumes that the factor C is approximately the same for both model setups. We consider this likely since we have observed qualitative and quantitative similarity as discussed in section 4.1. The estimated overall "effective viscosity" for the oceanic plate, $\bar{\mu}_{oc}^{eff}$, is about 7×10^5 Pa s. This number is sensitive to the measurement of the radius of curvature and higher than the measured viscosity for the silicon putty ($\approx 7 \times 10^4$ Pa s; Table 2). We interpret the latter as a result of the presence of a stiffer upper sand layer that increases the bending resistance and use $\bar{\mu}_{oc}^{eff}$ to estimate the buoyancy number for the laboratory experiments. The value we get is $F \approx 15.7$ for the reference model (Table 1).

4.4. Comments on the Numerical Results

Two additional issues can be addressed with the numerical experiments, the effect of the aspect ratio and that of a weak zone. Changing the aspect ratio of the computational domain to 1 by 4 or 2 by 4 leads to a delayed initiation of subduction and thus a shift in the slab depth versus time curves of ~10–15 Myr. This is due to the way gravitational instabilities form in our models. They are advected in the upper oceanic plate and have to travel some distance to assist in the initiation of downwelling at the plate boundary. Another factor which might be of influence, but is difficult to quantify, is the effect of a longer oceanic plate on the work done by deflecting streamlines which could further delay the initiation of subduction. Hence the individual data points that we present are dependent on the geometry chosen for the model and the wavelength of the convective instabilities that result. However, our conclusions concerning the physical mechanisms of subduction are not affected, and our general findings are confirmed by all models.

The effect of a preexisting fault at the plate boundary has been investigated by means of the introduction of a fixed 42 km by 42 km weak zone characterized by a 100-fold drop in viscosity. This configuration causes a change in model behavior only insofar as the slab dips at shallower angle at the start. When it reaches the bottom, it has steepened, and the shape of the subduction zone is similar to the other models. The absolute velocity of subduction is initially comparable to the ones observed in models without a weak zone and increases to ~140% during the final stages before the slab slows down. We note that the small effect that we find might be biased by our velocity boundary conditions and could be expected to increase with a larger weak zone.

5. Interpretation of the Experimental Results

The style of subduction and its influence on the state of stress in the overriding plate represent a complex problem in plate tectonics, and many models have been proposed (for a review see *Jarrard* [1986]). In our experiments, subduction is mostly controlled by the buoyancy number. We will now interpret the results by tracing the the slab trajectory from the surface to the bottom of the upper mantle and comparing our findings to previous models and examples from nature.

5.1. Nucleation and Development of Slabs

We model subduction as a purely viscous process, assuming that the slab behaves as a fluid over geological timescales. Within the investigated parameter range the deformation is localized at the boundary due to the presence of a stiff resisting upper plate. Subduction does not initiate for F below a threshold: in this case the deformation is characterized by low-angle underthrusting of the oceanic plate, by thickening and collision at the trench, and, in the laboratory experiments, by diffuse folding of the entire oceanic plate [*Faccenna et al.*, 1999b]. If we express the F threshold as a viscosity contrast between ocean and mantle, we arrive at an upper value of ~750 for the numerical experiments.

This finding is in agreement with the range predicted by *Conrad and Hager* [1997] and indicates a rather low effective lithospheric viscosity.

Even though we are not concerned with a force balance for subduction initiation, the stresses that result from our prescribed convergence boundary condition are of interest. As Figures 2, 4, and 5 indicate, nondimensionalized values are ~15 in the middle part of the oceanic plate. This gives 11.3 MPa and 1.13×10^{12} N/m for a 100-km-thick lithosphere (Table 1). While this number depends on the choice for the absolute viscosity value, it is in the range that can result from ridge push forces [e.g., *McKenzie*, 1977].

For F above the initiation threshold the slab nucleates as a large instability, growing at a slow rate during the first 10–20 Myr. Afterward, the instability narrows and evolves, following the mantle trajectories and resembling the shape of a slab. The initial growth rate of the instability and the velocity of subduction that follows depend upon the buoyancy number; that is, for a given convergence velocity, they are proportional to the density contrast but inversely proportional to the viscosity of the oceanic plate.

5.1.1. The velocity of subduction. During the first stages of deformation for both numerical and laboratory models the subduction speed is only a small percentage of the velocity of convergence u_r. Afterward, the slab accelerates until its speed becomes comparable to the velocity of convergence and the tip reaches the bottom at ~40–50 Myr and 20–30 Myr in numerical and laboratory reference experiments, respectively. A common feature of all experiments is the exponential increase of the subduction rate and its dependence upon F while the scaling relation (4) can be used to fit both numerical and laboratory data for free subduction (compare section 4.3). Furthermore, the dependence of the subduction rate on the buoyancy number F indicates that the viscosity in our scaling law (3) is indeed the viscosity of the oceanic plate (compare section 4.2), and numerical experiments show that most of the viscous dissipation takes place in the trench region. Therefore we conclude in agreement with *Conrad and Hager* [1997] that the major resisting force in our model is the viscous drag, mainly due to the bending of the slab. Thus we can infer that the resistance exerted by the mantle along the sides and the leading edge of the slab plays a subordinate role, since the effect of its viscosity can be neglected in comparison to that of the oceanic plate.

5.1.2. Comparison with nature and previous models. Previous laboratory and numerical models dealing with the long-term evolution of slabs sinking in the upper mantle either start with a predefined slab [e.g., *Kincaid and Olson*, 1987] or assume the presence of a preexisting fault zone crosscutting the whole lithosphere [e.g., *Shemenda*, 1993; *Zhong and Gurnis*, 1995; *Moretta and Sabadini*, 1995; *Hassani et al.*, 1997]. In the latter class of models the subduction speed depends on the velocity of convergence and on the predefined characteristics of the weak zone [*King and Hager*, 1990]. However, the velocity field observed in the numerical models of viscous slabs sinking into the mantle [*Moretta and Sabadini*, 1995; *Zhong and Gurnis*, 1995] is consistent with our results. Since the deformation of a Newtonian fluid as in our experiments is more diffuse than that of a power law material [e.g., *King and Hager*, 1990], we expect that the localization, the growth, and the rate of subduction for a power law fluid will be more accentuated, further enhancing the time-dependent increase in the subduction velocity.

In nature, the lack of unambiguous present-day examples of trench nucleation and the difficulty in establishing the age of subduction do not allow us to verify this prediction directly. In some cases, subduction seems to initiate slowly, as in the central Mediterranean [*Faccenna et al.*, 1999a], whereas in other areas, as in New Zealand, subduction developed rapidly [*Stern and Holt*, 1994]. Several parameters, such as the lateral propagation of the trench and the velocity of convergence, can determine the infant stage of subduction. However, the present-day velocities of most slabs, estimated by summing up the velocity of plate motion and the velocity of trench migration, are usually of the order of 3–10 cm/yr [e.g., *Jarrard*, 1986; *Otsuki*, 1989; *Rodkin and Rodnikov*, 1996]. This value refers to subduction zones where thousands of kilometers of oceanic lithosphere have been consumed during the last 100 Myr [e.g., *Cox et al.*, 1989]. In our time-dependent simulations we obtain similar velocities during the final stage of subduction, confirming the validity of our approach. If our scenario is applicable to Earth, the slow growth of the slab during the first stage of subduction should be taken into account in paleotectonic reconstruction.

Finally, the absence of a predefined and discrete subduction fault zone in our model implies that the upper plate is eroded and partially subducted [cf. *Tao and O'Connell*, 1992]. This process is confined to the lower layer of the overriding plate in the numerical experiments, while the fraction of material entering the trench from both parts of the overriding plate ranges from 10% to 30% of the total amount of subducted material in the laboratory. These numbers might be higher but are of the same order of magnitude as those estimated for Earth. In fact, trench subsidence and volcanic arc retreat as defined for some of the trenches on the Pacific ring indicate that the overriding arc is usually eroded at a rate of 8–10 km/Myr (for a review, see *Lallemand* [1995]).

5.2. The Style of Subduction and Trench Migration

In both numerical and laboratory experiments, contrasting styles of subduction have been observed as a function of the buoyancy number F. For low F the slab is thicker and sinks at low angle, and the trench

migrates toward the upper plate accompanied by compression. For high F where subduction is favored, the slab is thinner and dips steeply, and the trench migrates toward the ocean, producing back arc extension in the upper plate. In general, back arc extension is observed in our models when the velocity of subduction and trench retreat is higher than the velocity of convergence (Figures 3b and 7b). In this case, the hinge of the subducting plate rolls back leading to the retreat of the trench and extension in the upper plate.

As discussed in section 4.2, trench migration can be enhanced by collapse of the lighter upper plate toward the subducting one. This causes back arc extension in all numerical experiments with $F > 14$ even during their first stage of deformation (see Figures 3a and 3b). This result is similar to the laboratory experiments shown by *Faccenna et al.* [1996] where trench migration and back arc extension are obtained when the upper plate collapses under its own weight toward the oceanic plate. Therefore the nature of the "trench suction" in our experiments is related to the gravitational torque exerted by the downwelling motion of the denser subducting plate and the collapse of the upper plate. This can lead to effective back arc extension when the horizontal push imposed by the plate convergence and the internal strength of the upper plate are overcome. The rate of trench migration ranges from 0.3 to 1 times the velocity of subduction. Our experiments indicate that a viscous slab, coupled to the upper plate can indeed produce extension or compression in the overriding plate as a result of the dynamical competition between driving (gravitational energy release) and resisting effects (viscous dissipation in the subducting plate).

5.2.1. Comparison with nature and previous models. Previous numerical models obtained comparable results using a viscoplastic rheology to simulate the subduction process and the related instantaneous state of stress of the upper plate [e.g., *Whittaker et al.*, 1992; *Giunchi et al.*, 1996]. In those experiments the stress in the upper plate depends mainly upon the equilibrium between the body forces and the coupling along a preexisting fault zone. That is, unlocking of the fault zone will result in an increase in subduction velocity producing an extensional horizontal relaxation of the upper plate. Other laboratory [*Shemenda*, 1993] and numerical [*Hassani et al.*, 1997] studies using elastoplastic rheology propose a different mechanism, connected to the suction hydrostatically produced along the subduction fault zone. In this latter class of models the nature of trench suction is directly related to the increase in curvature and dip of the slab during its sinking into the mantle, which causes a downward force on the rigid subduction fault. Our models are in contrast to these studies since they show that trench migration can result from a viscous flow in a continuous medium with viscosity and density heterogeneities.

Another class of models supports the idea that trench suction is related to a corner flow caused by the drag exerted on the mantle by the sinking slab [e.g., *Andrews and Sleep*, 1974; *Bodri and Bodri*, 1978; *Toksoz and Hsui*, 1978]. Mantle drag and corner flow play a minor role in our experiments as trench migration occurs even before the slab starts sinking into the mantle. Furthermore, we find that mantle drag is not effective in determining the fate of the slab since viscous dissipation alone can account for the resisting effects (see section 5.1.1).

In nature, back arc compression or extension are well-documented end-members of more complex tectonic situations, showing variations both in space and time [*Uyeda and Kanamori*, 1979]. Kinematic models indicate that back arc extension can be connected with the absolute [*Chase*, 1978] or relative motion of plates [*Dewey*, 1980]. Hence, when the velocity of trench retreat (possibly related to the body force on the descending slab) overcomes the velocity of convergence, the upper plate is submitted to extension and vice versa. These models seem appropriate for most natural cases, even if exceptions do exist [*Taylor and Karner*, 1983]. Despite this, the way in which the two plates interact and the mechanism of force transmission from the subducting slab toward the upper plate are still poorly understood [*Taylor and Karner*, 1983]. On the basis of our results with a fixed upper plate and no background flow, we suggest that overriding plate compression or extension can be predicted using the buoyancy number F. It is difficult to test whether or not this mechanism can be applied to nature and to what extent other effects such as that of a background mantle flow [e.g., *Becker et al.*, 1998] matter. However, the velocities of trench migration and back arc extension in our experiments are in good agreement with the values observed in nature, where the velocity of back arc spreading is about half that of subduction [*Rodkin and Rodnikov*, 1996].

5.3. Dip of the Slab

In both numerical and laboratory experiments the subduction angle increases until the slab reaches the transition zone. This again suggests that subduction is a time-dependent phenomenon and poorly characterized by steady state parameters. In laboratory experiments the velocity of steepening ranges from ~1–2°/h, corresponding to 2°–4°/Myr in nature, and is proportional to F. While the steepening rates given by *Moretta and Sabadini* [1995] are twice as high, a comparison of models with Earth is difficult, in general, as subduction in nature is long-lived and possibly interacts with density or viscosity barriers such as at 670km [*Jarrard*, 1986].

With the boundary conditions under consideration, shallowing of the slab can only be obtained by anchoring the slab at a deep transition zone. In this case, the dip of the slab changes as a function of the velocity of trench motion. If the trench migrates oceanwards, as in experiment 7, the hinge of the slab rolls back with respect to its fixed tip inducing a decrease of the sub-

duction angle. This result agrees with previous simulations using a more realistic increase in viscosity at the upper-lower mantle boundary [*Tao and O'Connell*, 1992; *Zhong and Gurnis*, 1995; *Griffiths et al.*, 1995]. Consistent with these models, we suggest that a shallow dipping subduction cannot be the result of the dynamic equilibrium between slab and upper mantle but other factors, such as interaction with a deep transition zone and/or background mantle flow, should operate.

5.4. Deformation Within the Slab

Our models indicate that the stress within the slab is usually downdip extension during its descent into the mantle regardless of the buoyancy number. When the slab reaches the transition zone, the area under tension is confined to the upper part of the slab, while the tip is submitted to compression. At half depth the stress field changes and decreases in magnitude forming a neutral downdip stress zone. Similar results have been obtained in earlier viscous flow models for the stress state in a fixed subduction geometry [*Vassiliou and Hager*, 1988] and the strain field for homogeneous viscosity [*Tao and O'Connell*, 1993]. Here we have demonstrated that self-consistent viscous flow models with viscosity heterogeneities can reproduce the stress pattern that is common for many subduction zones [*Isacks and Molnar*, 1971], even if the position of the neutral downdip stress zone might depend upon the slab morphology [*Zhou*, 1990] and the effect of phase transitions could complicate the picture [e.g., *Yoshioka et al.*, 1997]. Our models support the interpretation that the seismicity in Benioff zones arises from a competition between slab-pull and slab impediment in the lower mantle [*Isacks and Molnar*, 1971; *Spence*, 1987].

6. Conclusion

Our results from numerical and laboratory experiments demonstrate that it is possible to explain the major observations for subduction zones in Earth, such as trench migration and the stress pattern within the slab, with viscous models based on density and viscosity heterogeneities between the tectonic plates. The style of subduction can be characterized by the buoyancy number which measures the importance of driving density contrasts versus resisting viscous dissipation. The existence of a threshold for subduction initiation yields an upper bound for the viscosity of the oceanic subducting plate. Our results support the view that subduction cannot be represented as a steady state process since the state of stress, the velocity, and the dip of the slab evolve in space and time during its descent into the upper mantle.

Acknowledgments. We would like to thank Dave Bercovici, Shije Zhong, and an anonymous reviewer for their helpful critiques of the original version of the typescript. T.W.B. thanks Simone Bethge for her kind support, James B. Kellogg and Paul Oxley for comments, and received funding from a DAAD "Doktorandenstipendium HSP–III." Laboratory experiments have been performed in the Experimental Tectonics Lab of Geosciences Rennes (France) and the University of Rome TRE (Italy). C.F. is particularly grateful to Jean P. Brun, Philippe Davy, and Jean J. Kermarrec of the Rennes Lab for their invaluable scientific collaboration during experiments and to Renato Funiciello for continuous encouragement. C.F. has been financially supported by CNR grant 203.05.18. Support by NSF is also acknowledged.

References

Andrews, D. J., and N. H. Sleep, Numerical modeling of tectonic flow behind Island Arc, *Geophys. J. R. Astr. Soc.*, *38*, 237–251, 1974.

Becker, T. W., C. Faccenna, and R. J. O'Connell, Mantle winds and back-arc spreading: The influence of background flow on subdution in the upper mantle (abstract), *Eos Trans. AGU*, *79*(45), Fall Meet. Suppl., F849, 1998.

Bevis, M., The curvature of Wadati-Benioff zones and the torsional rigidity of subducting plates, *Nature*, *323*, 52–53, 1986.

Bevis, M., Seismic slip and down dip strain rate in Wadati-Benioff zones, *Science*, *240*, 1317–1319, 1988.

Bodri, L., and B. Bodri, Numerical investigation of tectonic flow in island-arc areas, *Tectonophysics*, *50*, 163–175, 1978.

Brace, W. F., and D. L. Kohlstedt, Limits on lithospheric stress imposed by laboratory experiments, *J. Geophys. Res.*, *85*, 6248–6252, 1980.

Chase, C. G., Extension behind island arcs and motion relative to hot spots, *J. Geophys. Res.*, *83*, 5385–5387, 1978.

Cloos, M., Lithospheric buoyancy and collisional orogenesis: subduction of oceanic plateaus, continental margins, island arcs, spreading ridges and seamounts, *Geol. Soc. Am. Bull.*, *105*, 715–737, 1993.

Conrad, C. P., and B. H. Hager, The role of plate bending and fault strength at subduction zones on plate dynamics (abstract), *Eos Trans. AGU*, *78*(46), Fall Meet. Suppl., F4, 1997.

Cox, A. M., G. Debiche, and D. C. Engebretson, Terrane trajectories and plate interaction along continental margins in the north Pacific basin, in *The Evolution of the Pacific Ocean Margins*, edited by Z. Ben-Avraham, pp. 20–35, Oxford Univ. Press, New York, 1989.

Cross, T. A., and R. C. Pilger, Controls of subduction geometry, location of magmatic arcs, tectonics of arc and back-arc regions, *Geol. Soc. Am. Bull.*, *93*, 545–562, 1982.

Davies, G. F., On the emergence of plate tectonics, *Geology*, *20*, 963–966, 1992.

Davy, P., and P. R. Cobbold, Experiments on shortening of a 4-layer model of the continental lithosphere, *Tectonophysics*, *188*, 1–25, 1991.

Dewey, J. F., Episodicity, sequence and style at convergent plate boundaries, in *The Continental Crust and its Mineral Deposits*, vol. 20, *Geol. Assoc. Can. Spec. Pap.*, 553–573, 1980.

Faccenna, C., P. Davy, J.-P. Brun, R. Funiciello, D. Giardini, M. Mattei, and T. Nalpas, The dynamics of back-arc extension: An experimental approach to the opening of the Tyrrhenian Sea, *Geophys. J. Int.*, *126*, 781–795, 1996.

Faccenna, C., D. Giardini, T. W. Becker, and R. J. O'Connell, History of subduction and backarc extension in the Central Mediterranean, *Geophys. Res. Abs.*, *1*(1), 79, 1999a.

Faccenna, C., D. Giardini, P. Davy, and A. Argentieri, Initiation of subduction at Atlantic type margins: In-

sights from laboratory experiments, *J. Geophys. Res.*, *104*, 2749–2766, 1999b.

Furlong, K. P., D. S. Chapman, and P. W. Alfeld, Thermal modeling of the geometry of subduction with implications for the tectonics of the overriding plate, *J. Geophys. Res.*, *87*, 1786–1802, 1982.

Giardini, D., and J. H. Woodhouse, Deep seismicity and modes of deformation in Tonga subduction zone, *Nature*, *307*, 505–509, 1984.

Giunchi, C., R. Sabadini, E. Boschi, and P. Gasperini, Dynamic models of subduction: Geophysical and geological evidence in the Tyrrhenian sea, *Geophys. J. Int.*, *126*, 555–578, 1996.

Gouillou-Frottier, L., J. Buttles, and P. Olson, Laboratory experiments on the structure of subducted lithosphere, *Earth Planet. Sci. Lett.*, *133*, 19–34, 1995.

Griffiths, R. W., R. I. Hackney, and R. D. van der Hilst, A laboratory investigation of effects of trench migration on the descent of subducted slabs, *Earth Planet. Sci. Lett.*, *133*, 1–17, 1995.

Gurnis, M., and B. H. Hager, Controls of the structure of subducted slabs, *Nature*, *335*, 317–321, 1988.

Hassani, R., D. Jongmans, and J. Chéry, Study of plate deformation and stress in subduction processes using two-dimensional numerical models, *J. Geophys. Res.*, *102*, 17,951–17,965, 1997.

Houseman, G. A., and D. Gubbins, Deformation of subducted oceanic lithosphere, *Geophys. J. Int.*, *131*, 535–551, 1997.

Hsui, A. T., Application of fluid mechanic principles to the study of trench back-arc systems, *Pure Appl. Geophys.*, *128*, 661–681, 1988.

Isacks, B., and M. Barazangi, Geometry of Benioff zones: Lateral segmentations and downward bending of subducted lithosphere, in *Island Arcs, Deep Sea Trenches, and Back-Arc Basins*, vol. 1, *Maurice Ewing Ser.*, edited by M. Talwani and W. C. Pitman III, pp. 99–114, AGU, Washington, D. C., 1977.

Isacks, B., and P. Molnar, Distribution of stresses in the descending lithosphere from a global survey of focal-mechanism solutions of mantle earthquakes, *Rev. Geophys.*, *9*, 103–175, 1971.

Jacoby, W. R., and H. Schmeling, Convection experiments and driving mechanism, *Geol. Rundsch.*, *24*, 217–284, 1981.

Jarrard, R. D., Relations among subduction parameters, *Rev. Geophys.*, *24*, 217–284, 1986.

Kincaid, C., and P. Olson, An experimental study of subduction and slab migration, *J. Geophys. Res.*, *92*, 13,832–13,840, 1987.

King, S. D., and B. H. Hager, The relationship betwenn plate velocity and trench viscosity in Newtonian and power-law subduction calculations, *Geophys. Res. Lett.*, *17*, 2409–2412, 1990.

King, S. D., and J. Ita, Effect of slab rheology on mass transport across a phase transition boundary, *J. Geophys. Res.*, *100*, 20,211–2022, 1995.

King, S. D., D. A. Raefsky, and B. H. Hager, ConMan: vectorizing a finite element code for incompressible two-dimensional convection in the Earth's mantle, *Phys. Earth Planet. Inter.*, *59*, 195–207, 1990.

Lallemand, S., High rates of arc consumption by subduction processes: Some consequences, *Geology*, *23*, 551–554, 1995.

Lenardic, A., and W. M. Kaula, A numerical treatment of geodynamic viscous flow problems involving the advection of material interfaces, *J. Geophys. Res.*, *98*, 8243–8260, 1993.

Luyendyk, B. P., Dip of downgoing lithospheric plates beneath island arcs, *Geol. Soc. Am. Bull.*, *81*, 3411–3416, 1970.

Martinod, J., and P. Davy, Periodic instabilities during compression or extension of the lithosphere, 1, Deformation modes from an analytical perturbation method, *J. Geophys. Res.*, *97*, 1999–2014, 1992.

Martinod, J., and P. Davy, Periodic instabilities during compression or extension of the lithosphere, 2, Analogue experiments, *J. Geophys. Res.*, *99*, 12,057–12,069, 1994.

McKenzie, D. P., The initiation of trenches: a finite amplitude instability, in *Island Arcs, Deep Sea Trenches, and Back-Arc Basins*, vol. 1, *Maurice Ewing Ser.*, edited by M. Talwani and W. C. Pitman III, pp. 99–114, AGU, Washington, D. C., 1977.

Molnar, P., and T. Atwater, Interarc spreading and cordillera tectonics as alternates related to the age of subducted oceanic lithosphere, *Earth Planet. Sci. Lett.*, *41*, 330–340, 1978.

Moretta, A. M., and R. Sabadini, The styles of Tyrrhenian subduction, *Geophys. Res. Lett.*, *22*, 747–750, 1995.

Otsuki, K., Empirical relationships among the convergence rate of plates, rollback rate of trench axis and island-arc tectonics: "Law of convergence rate of plates", *Tectonophysics*, *159*, 73–94, 1989.

Oxburgh, E. R., and D. L. Turcotte, The physico-chemical behaviour of the descending lithosphere, *Tectonophysics*, *32*, 107–128, 1976.

Ranalli, G., and D. C. Murphy, Rheological stratification of the lithosphere, *Tectonophysics*, *132*, 291–295, 1986.

Ricard, Y., C. Doglioni, and R. Sabadini, Differential rotation between lithosphere and mantle: A consequence of lateral mantle viscosity variations, *J. Geophys. Res.*, *96*, 8407–8415, 1991.

Rodkin, M. V., and A. G. Rodnikov, Origin and structure of back-arc basins: New data and model discussion, *Phys. Earth Planet. Inter.*, *93*, 123–131, 1996.

Russo, R. M., and P. G. Silver, Trench-parallel flow beneath the Nazca plate from seismic anisotropy, *Science*, *263*, 1105–1111, 1994.

Sacks, I. S., The subduction of young lithosphere, *J. Geophys. Res.*, *88*, 3355–3366, 1983.

Shemenda, A. I., Subduction of the lithosphere and back arc dynamics: Insights from physical modeling, *J. Geophys. Res.*, *98*, 16,167–16,185, 1993.

Spence, W., Slab pull and the seismotectonics of subducting lithosphere, *Rev. Geophys.*, *25*, 55–69, 1987.

Stacey, F. D., *Physics of the Earth*, Kenmore, Australia, 3rd ed., Brookfield, 1992.

Stern, T. A., and W. E. Holt, Platform subsidence behind an active subduction zone, *Nature*, *368*, 233–236, 1994.

Stevenson, D. J., and J. S. Turner, Angle of subduction, *Nature*, *270*, 334–336, 1972.

Tao, W. C., and R. J. O'Connell, Ablative subduction: A two-sided alternative to the conventional subduction model, *J. Geophys. Res.*, *97*, 8877–8904, 1992.

Tao, W. C., and R. J. O'Connell, Deformation of a weak subducted slab and variation of seismicity with depth, *Nature*, *361*, 626–628, 1993.

Taylor, B., and G. D. Karner, On the evolution of marginal basins, *Rev. Geophys.*, *21*, 1727–1741, 1983.

Toksoz, M. N., and A. T. Hsui, Numerical studies of back-arc convection and the formation of marginal basins, *Tectonophysics*, *50*, 177–196, 1978.

Tovish, A., and G. Schubert, Island arc curvature, velocity of continents and angle of subduction, *Geophys. Res. Lett.*, *5*, 329–332, 1978.

Turcotte, D. L., and G. Schubert, *Geodynamics. Applications of Continuum Physics to Geological Problems*, John Wiley, New York, 1982.

Uyeda, S., and H.-J. Kanamori, Back-arc opening and the mode of subduction, *J. Geophys. Res.*, *84*, 1049–1061, 1979.

van den Berg, A. P., and D. A. Yuen, The role of shear heating in lubricating mantle flow, *Earth Planet. Sci. Lett.*, *151*, 33–42, 1997.

van der Hilst, R. D., E. R. Engdahl, R. Spakman, and T. Nolet, Tomographic imaging of subducted lithosphere below northwest Pacific island arcs, *Nature*, *353*, 47–53, 1991.

Vassiliou, M. S., and B. H. Hager, Subduction zone earthquakes and stress in slabs, *Pure Appl. Geophys.*, *128*, 547–624, 1988.

Weijermars, R., Flow behavior and physical chemistry of bouncing putty and related polymers in view of tectonic laboratory applications, *Tectonophysics*, *124*, 325–358, 1992.

Whittaker, A., and M. H. P. Bott, and G. D. Waghorn, Stress and plate boundary forces associated with subduction plate margins, *J. Geophys. Res.*, *97*, 11,933–11,944, 1992.

Wortel, R., Seismicity and rheology of subducted slabs, *Nature*, *296*, 553–556, 1982.

Yoshioka, S., R. Daessler, and D. A. Yuen, Stress fields associated with metastable phase transitions in descending slabs and deep-focus earthquakes, *Phys. Earth Planet. Inter.*, *104*, 345–361, 1997.

Zhong, S., and M. Gurnis, Mantle convection with plates and mobile, faulted plate margins, *Science*, *267*, 838–842, 1995.

Zhou, H.-W., Observations on earthquake stress axes and seismic morphology of deep slabs, *Geophys. J. Int.*, *103*, 377–401, 1990.

Th. W. Becker and R. J. O'Connell, Harvard University, Department of Earth and Planetary Sciences, 20 Oxford St., Cambridge, MA 02138. (becker@eps.harvard.edu; oconnell@geophysics.harvard.edu)

C. Faccenna, Dipartimento di Science Geologiche, Universitá di Roma Tre, Largo S. R. Murialdo 1, Rome 00146, Italy. (faccenna@uniroma3.it)

D. Giardini, Institute of Geophysics, ETH, 8093 Zurich, Switzerland.

(Received June 30, 1998; revised February 26, 1999; accepted April 19, 1999.)